Transverse- and Axial-Flux Permanent Magnet Machine With C-Type SMC Stator: A Solution for Ultra-Flat Applications

Ren Tsunata, *Member, IEEE*, Masatsugu Takemoto, *Member, IEEE*, Jun Imai, *Member, IEEE*, Tatsuya Saito, and Tomoyuki Ueno

***Abstract*—This article proposes a novel transverse- and axial-flux permanent magnet machine (T-AFPM) using a C-type stator core for reducing system size via an ultra-flat shape. With an axial length of only 19.7 mm, this ultra-flat shape contributes markedly to reducing system size in industrial applications such as water pumps. In general, AFPMs are suitable for a flat shape because of their high torque density with a short axial length. However, it is difficult to use conventional AFPMs to achieve an ultra-flat shape because of structural problems and insufficient performance. By contrast, the proposed T-AFPM achieves a highly manufacturable structure, high efficiency, and the required output power despite its extremely short axial length. Herein, the T-AFPM is compared with conventional AFPMs with various configurations by means of three-dimensional finite-element analysis, and experiments on a T-AFPM prototype are reported. From the simulation and experimental results, the proposed T-AFPM shows high efficiency (IE5 class), the required output power, and suitable structural properties for an ultra-flat shape.**

***Index Terms*—Axial-flux machine, coreless rotor structure, C-shaped core, efficiency (IE5 class), permanent magnet synchronous machine (PMSM), short axial length, soft magnetic composite (SMC), transverse-flux machine, ultra-flat shape.**

I. Introduction

In many applications such as industrial and traction applications, electrical machines with a flat shape are often required to reduce system size. Therefore, the aim of the research reported herein is to develop a 700-W electrical machine with an axial length of less than 20 mm for extremely compact systems in industrial applications. Moreover, because the production volume of 700-W electrical machines for applications such as water pumps is very large [1], also required is highly efficient and low-cost mass production. Furthermore, because many industrial electrical machines need to operate at high speed and with high torque [2], high efficiency is required under those conditions. In summary, the goal is to develop a 700-W electrical machine with an ultra-flat shape, high efficiency at high speed, and a highly manufacturable structure.

Commonly used radial flux permanent magnet machines (RFPMs) are not suitable for flat configurations because they have axial coil ends that do not contribute to torque generation. In contrast, axial-flux permanent magnet machines (AFPMs) attract attention because of their high torque density with a flat shape. For decades, many research groups have investigated AFPMs with various structures. However, conventional AFPMs are not suitable for an ultra-flat shape with an axial length of less than 20 mm because of manufacturing and structural constraints. For example, a single-stator double-rotor (SSDR) structure is not suitable for ultra-flat structures because there are air gaps above and below the two rotors. A double-stator single-rotor (DSSR) structure has thin components, and the manufacturability is significantly reduced, especially for stator cores using soft magnetic composite (SMC). A single-stator single-rotor (SSSR) structure can generate high torque even with an ultra-flat structure, but a large axial electromagnetic force is generated, which causes noise and mechanical loss, especially in the high-speed region of the target. In addition, with these conventional AFPMs, it is difficult to achieve sufficient mechanical strength due to a large rotor diameter in ultra-flat shape. Accordingly, to meet the above requirements, this article proposes a novel transverse- and axial-flux permanent magnet machine (T-AFPM) with a C-type core and a coreless rotor structure. Fig. 1 shows a three-dimensional (3-D) model of the proposed T-AFPM with an axial length of 19.7 mm for ultra-flat applications, which simultaneously achieves an output power of more than 700 W, high efficiency (IE5 class) [3], and a highly manufacturable structure despite its ultra-flat shape.

In the proposed T-AFPM, there are magnetic flux paths in both the transverse and axial directions. Transverse-flux permanent magnet machines (TFPMs) are comprehensively reviewed in [4]. According to [4], the proposed T-AFPM can also be referred to as an axial-gap-type transverse-flux machine. In TFPMs, the proposed structure combining a C-shaped core and a coreless rotor to achieve high performance with an ultra-flat structure has not been reported. In previous work, our research group proposed the T-AFPM and evaluated its basic characteristics (e.g., torque) [5]. However, that work was lacking

Received 8 July 2025; revised 29 September 2025; accepted 30 October 2025. Date of publication 15 December 2025; date of current version 11 March 2026. *(Corresponding author: Ren Tsunata.)*

Ren Tsunata, Masatsugu Takemoto, and Jun Imai are with the Graduate School of Environmental, Life, Natural Science and Technology, Okayama University, Okayama 700-8530, Japan (e-mail: tsunata@okayama-u.ac.jp).

Tatsuya Saito and Tomoyuki Ueno are with the Sumitomo Electric Sintered Alloy Ltd., Osaka 554-0024, Japan.

Digital Object Identifier 10.1109/TIE.2025.3629360

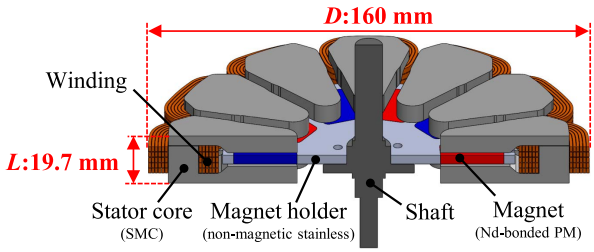

Fig. 1. Proposed transverse- and axial-flux machine employing C-type SMC core.

in reference to previous research, a detailed comparison with conventional AFPMs, and experimental results. Accordingly, this article covers the following topics: an investigation of the aspect ratio and sizes of conventional AFPMs (Section II); a comprehensive comparison between conventional AFPMs and the proposed T-AFPM with an ultra-flat shape with an axial length of 19.7 mm (Section III); experimental verification of a prototype of the proposed T-AFPM (Section IV); discussion about the effectiveness of the proposed T-AFPM (Section V).

II. Structural and Size Differences Between Conventional AFPMs and the Proposed T-AFPM

A. Structural Problems of Ultra-Flat AFPMs

AFPMs can be classified by their structures into a SSSR [6], [7], a DSSR [8], [9], SSDR [10], [11], and multistator multirotor (MSMR) [12], [13]. Fig. 2 shows schematics of AFPMs with each of these structures, as well as the proposed T-AFPM, and it indicates the problems of conventional AFPMs with an ultra-flat shape.

First, with an AFPM with the SSSR structure (SSSR-AFPM) as shown in Fig. 2(a), it is relatively easy to achieve a flat shape because there are only a few components in the axial direction. However, large eddy current loss is likely to occur in the rotor back core at high rotational speed, and it has an asymmetric configuration in the axial direction. Consequently, both the rotor and stator experience large axial force that causes noise and large mechanical loss, thereby reducing the efficiency and bearing lifetime.

Second, a DSSR-AFPM as shown in Fig. 2(b) is a reasonable structure for high-speed applications because it does not have the rotor back core. However, in an ultra-flat DSSR-AFPM with an axial length of less than 20 mm, the stator back core is extremely thin, and so mass production is difficult.

Third, an SSDR-AFPM as shown in Fig. 2(c) can achieve good torque characteristics with an ordinary aspect ratio. However, an ultra-flat SSDR-AFPM has the following critical problems: large eddy current loss at high speed (as with an SSSR-AFPM); many air gaps increasing the axial length; thin permanent magnets (PMs) with a high risk of demagnetization.

By contrast, an ultra-flat T-AFPM with a C-type stator as shown in Fig. 2(d) is an improvement on the above designs. The stator core is thicker than in the other models because the windings are not in the axial direction, and so the PMs are also thicker. Therefore, both manufacturability and durability against demagnetization are higher for the T-AFPM than for the

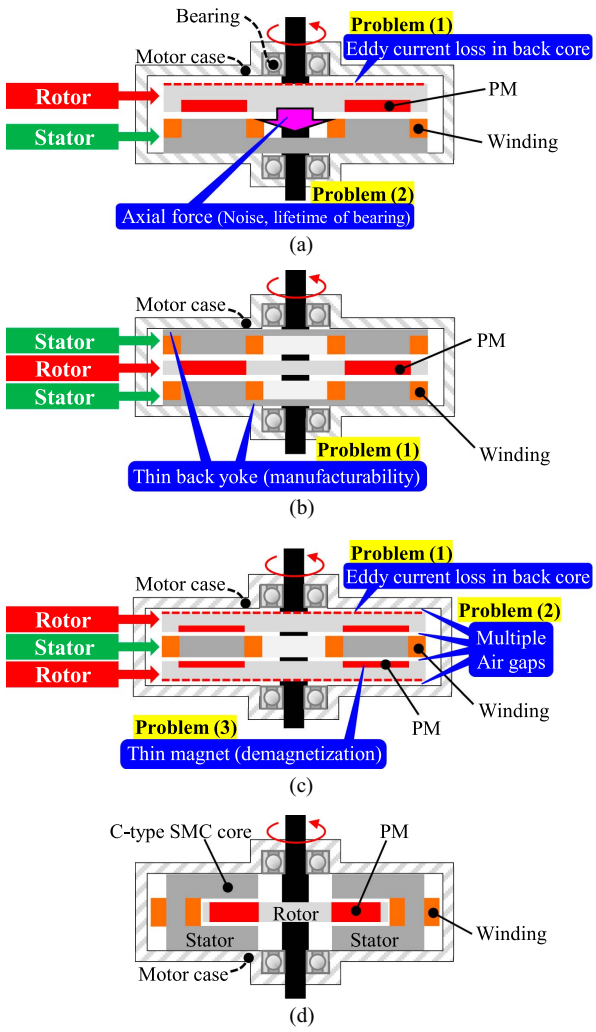

Fig. 2. Difference of each model and problems of three conventional AFPMs in ultra-flat shape. (a) SSSR-AFPM. (b) DSSR-AFPM. (c) SSDR-AFPM. (d) Proposed T-AFPM having C-type core.

other models with an ultra-flat shape. Furthermore, the T-AFPM has a symmetric configuration in the axial direction, thereby alleviating the axial-force problem of an SSSR-AFPM.

B. Aspect Ratio and Size of T-AFPM

Herein, the aspect ratio k is defined as follows:

$$k = \frac{L}{D} \tag{1}$$

where L and D are the axial length and outer diameter, respectively, of an electrical machine without its case. Fig. 3 shows the axial lengths and outer diameters of existing AFPMs investigated in many references and the proposed T-AFPM, as well as aspect-ratio lines and volume lines corresponding to $k = 0.1$–0.5 and 0.1–3.0 L, respectively. As can be seen, most existing AFPMs are designed with $k = 0.2$–0.4 regardless of their structures and machine size. Some SSSR-AFPMs have relatively low aspect ratio or short axial length compared with DSSR-, SSDR-, and MSMR-AFPMs, but the proposed T-AFPM has the shortest axial length (19.7 mm) and the lowest

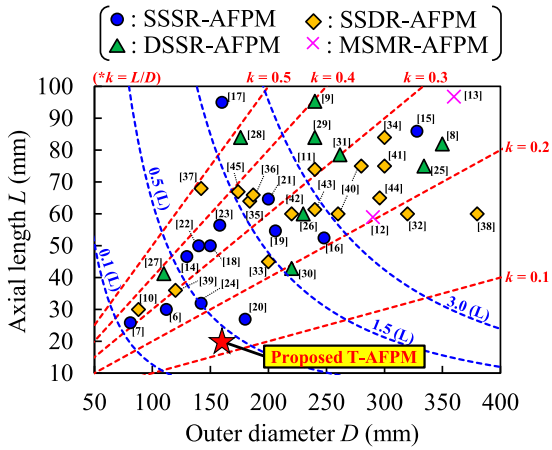

Fig. 3. Advantage in short axial length of the proposed T-AFPM and survey results of aspect ratio of conventional AFPMs ([6]–[45]).

TABLE I
PARAMETERS AND DESIGN CONSTRAINTS OF COMPARATIVE MODELS

Parameters	Values	Parameters	Values
Number of poles/slots	10p/12s	Required output power	> 700 W
Machine volume	0.39 L	Maximum speed	6000 rpm
Axial length L	19.7 mm	Rated current density	4 Arms/mm^2
Outer diameter D	160 mm	Rated inverter current	8.0 arms
Aspect ratio k (L/D)	0.12	DC-bus voltage	<100 V
Air-gap length	1.0 mm		

aspect ratio (0.12) in Fig. 3. Objectively, it is therefore the case that the proposed T-AFPM has an extremely flat structure.

III. Comprehensive Comparison Between Conventional AFPMs and Proposed T-AFPM

A. Comparative Models and Conditions

Fig. 4 shows an SSSR-AFPM, a DSSR-AFPM, and the proposed T-AFPM as the models for comparison by 3-D finite-element analysis (FEA), and Table I lists their design constraints. No SSDR-AFPM or the MSMR-AFPM was considered because clearly neither is suitable for an ultra-flat shape. As mentioned earlier, the axial length of each model is 19.7 mm for an ultra-flat shape; also, the outer diameter is 160 mm, giving an aspect ratio of 0.12. The target output power is at least 700 W at a maximum rotational speed of 6000 rpm, and the rated current density is 4.0 Arms/mm^2 because of the lack of a cooling system.

All models use neodymium (Nd)-bonded PMs with near-zero conductivity, thereby restraining the eddy current loss therein at high speed [27]; for better comparison, the all models have the same magnet weight of 89.2 g. However, the residual magnetic flux density B_r of the Nd-bonded PM is approx. 30% lower than that of neodymium sintered permanent magnets (Nd-sintered PM), and hence, the torque density also decreases. However, it is necessary to use Nd-bonded PMs for continuous operation at high speeds in this application. The rotors of the DSSR-AFPM and the proposed T-AFPM have only Nd-bonded PMs

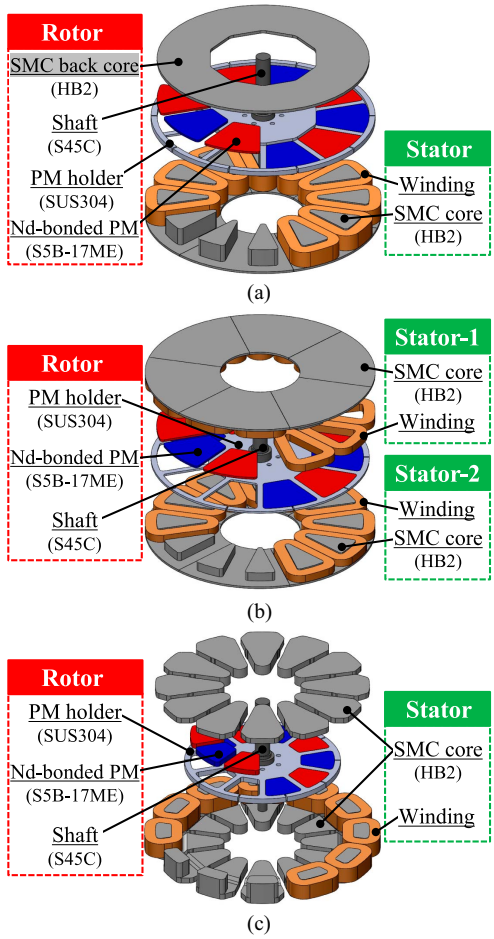

Fig. 4. Comparative models for 3-D-FEA. (a) SSSR-AFPM. (b) DSSR-AFPM. (c) Proposed T-AFPM.

and nonmagnetic stainless PM holders (namely, there is no magnetic core), as so this rotor structure is therefore referred as being coreless; the coreless rotor structure helps to reduce the eddy current loss and thickness of the rotor because there is no back core [46]. Additionally, the stator core of each model is made of an SMC because of the 3-D magnetic flux path in the stator; the chosen SMC (HB2; Sumitomo Electric Industries Ltd.) has a good iron loss property [47], [48]. Only the SSSR-AFPM has the rotor back core made of SMC with which to construct an effective magnetic path. If the rotor back core of the SSSR-AFPM were to be made of structural materials such as S45C, large eddy current loss would occur therein. However, it is difficult to manufacture thin components made of SMC, thereby leading to poor manufacturability for the SSSR-AFPM with an ultra-flat shape.

Table II details the parameters of the comparative models shown in Fig. 5. For better comparison, there are two DSSR-AFPMs with different winding structures, as shown in Fig. 5(b) and (c). DSSR-AFPM-1 and -2 have round and rectangular copper wires, respectively. The proposed T-AFPM [see Fig. 4(c)] has rectangular copper wires to enhance torque density as shown in Fig. 5(d). The rectangular wires have a higher coil fill factor compared to the round wires. As mentioned earlier,

TABLE II
DETAILED PARAMETERS AND DIMENSIONS OF COMPARATIVE MODELS

Parameters	SSSR-AFPM	DSSR-AFPM-1	DSSR-AFPM-2	Proposed T-AFPM
Stator structure	Single	Double	Double	C-type
Winding type	Round	Round	Rectangle	Rectangle
Coil fill factor	40%	40%	70%	70%
PM weight	89.2 g	89.2 g	89.2 g	89.2 g
Rotor diameter	152 mm	152 mm	152 mm	105.8 mm
PM thickness t_{pm}	1.5 mm	1.5 mm	1.5 mm	3.7 mm
Stator core thickness $t_{\mathrm{yoke\_}s}$	1.5 mm	1.5 mm	1.5 mm	4.0 mm
Rotor core thickness $t_{\mathrm{yoke\_}r}$	2.0 mm	-	-	-

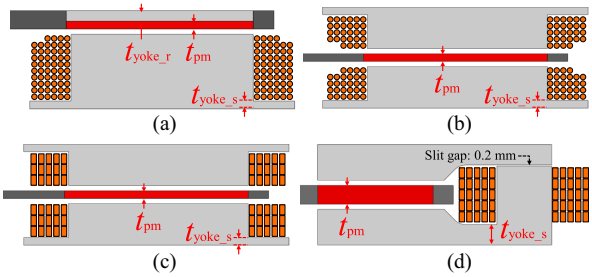

Fig. 5. Schematic representation of comparative models.

the PM thickness t_{pm} and the yoke thickness $t_{\mathrm{yoke\_}s}$ of the proposed T-AFPM are larger than those of DSSR-AFPM-1 and DSSR-AFPM-2. Hence, the proposed T-AFPM has better manufacturability. The dimensional parameters such as t_{pm} and $t_{\mathrm{yoke\_}s}$ of the comparative models were determined through a parametric study for maximizing the torque. The C-type core of the proposed T-AFPM is axially divided and there is a slit gap of 0.2 mm between them to insert winding.

B. Torque Performance and Power Factor

This section evaluates the torque of the four comparative AFPMs and discusses the causes of their torque differences. Fig. 6 shows the torque waveforms of the four models at 6000 rpm and 4.0 Arms/mm^2. The average torque of DSSR-AFPM-1 with round wires is the smallest, but its torque ripple is the largest. By contrast, DSSR-AFPM-2 with rectangular wires has the largest torque of the four models because its magnetomotive force is the highest for a given current density. For the proposed T-AFPM, its average torque is relatively high at 1.11 N·m. This value corresponds to ca. 700 W as the target power. Therefore, the proposed T-AFPM can achieve the required power at the rated current density of 4.0 Arms/mm^2. The SSSR-AFPM can generate torque slightly higher torque than that of the proposed T-AFPM.

First, to discuss the factors behind the torque differences among the four AFPMs, the effect of the aspect ratio k is evaluated. As mentioned in Fig. 3, the aspect ratio $k = 0.12$ considered in this article is an extremely flat structure. Fig. 7 shows change in magnet shape of SSSR- and DSSR-AFPM with respect to aspect ratio k. The machine volume and magnet weight are constant, and the aspect ratio k is changed in the range from 0.12 to 0.81. Fig. 7(a) shows representative models

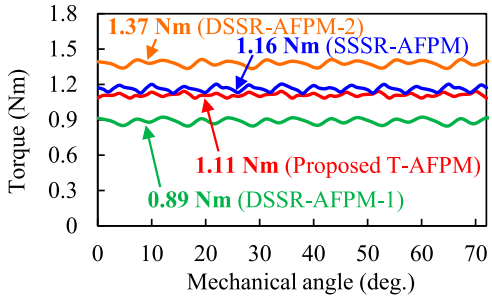

Fig. 6. Torque waveforms of three comparative models at rated current density of 4.0 Arms/mm^2 (@6000 rpm).

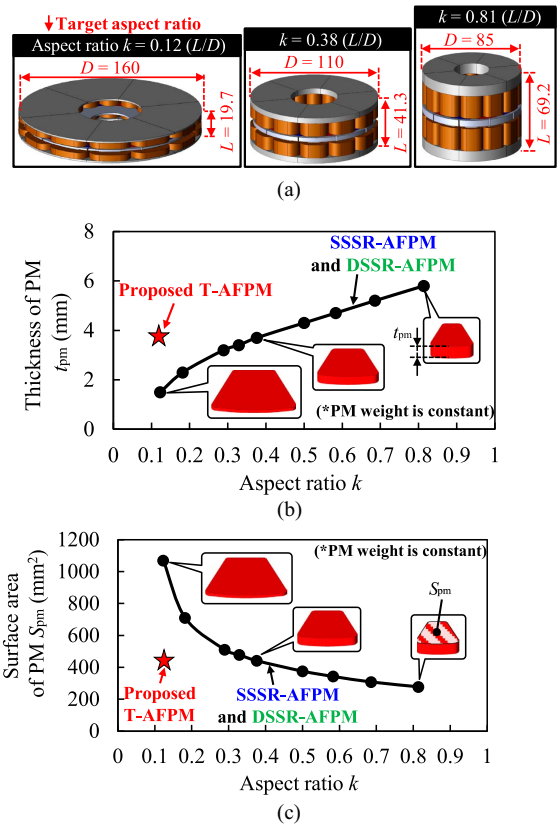

Fig. 7. Change in magnet shape of SSSR- and DSSR-AFPMs with respect to aspect ratio k. (a) Representative DSSR models with different aspect ratio k. (b) Thickness of magnet t_{pm} versus aspect ratio. (c) Surface area of magnet s_{pm} versus aspect ratio.

of DRRS-AFPM with several aspect ratios. Fig. 7(b) and (c) shows the magnet thickness t_{pm} and surface area S_{pm} for each aspect ratio, respectively. In addition, in Fig. 7(b) and (c), the magnet shape is the same for SSSR-AFPM and DSSR-AFPM. As shown in Fig. 7(b), when the outer diameter increases and the aspect ratio k decreases, the AFPMs become flatter and the magnet thickness t_{pm} decreases. Conversely, the magnet surface area S_{pm} increases as aspect ratio k decreases because the magnet weight is constant, as shown in Fig. 7(c).

The torque generation area can be increased by large surface area S_{pm}, while when the magnet thickness t_{pm} is small, the magnetic flux density in the air gap decreases. In the ultra-flat

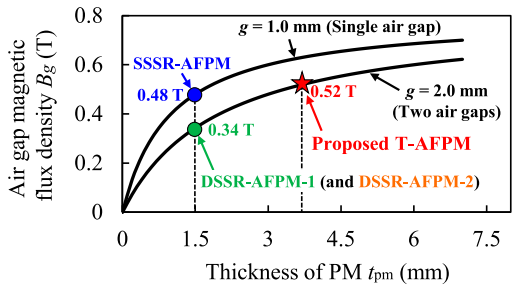

Fig. 8. Air gap magnetic flux density B_g against magnet thickness t_{pm} in different air gap length g.

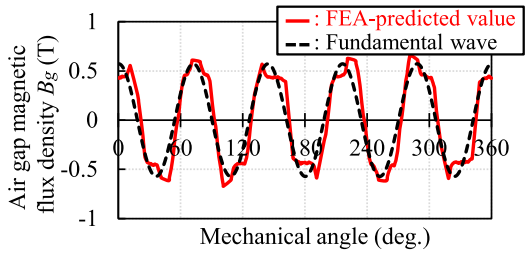

Fig. 9. Air gap magnetic flux density of proposed T-AFPM calculated by 3-D-FEA under no-load condition.

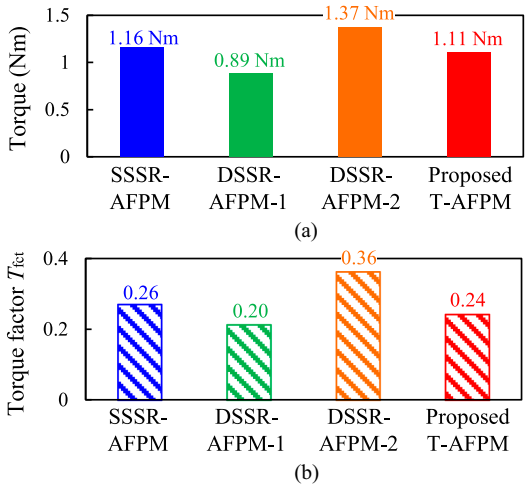

Fig. 10. Comparison of the four AFPMs in terms of average torque. (a) Average torque obtained by 3-D-FEA. (b) Average torque factor T_{fct} calculated by (3).

structure ($k = 0.12$) targeted in this article, the magnets of the SSSR- and DSSR-AFPMs have a large magnet surface area S_{pm}, but the thickness t_{pm} is very small at 1.5 mm. Fig. 7(b) and (c) also include the magnet parameters of the proposed T-AFPM, and although the surface area S_{pm} is smaller than that of conventional AFPMs with an ultra-flat structure ($k = 0.12$), the thickness t_{pm} is 3.7 mm, which is about 2.5 times larger. This is because the proposed T-AFPM has no windings above or below the magnet due to its structure, and the rotor diameter is also small.

The magnetic flux density in the air gap B_g can be predicted using the following formula:

$$B_g = \frac{t_{pm}}{t_{pm} + g} B_r \tag{2}$$

where g is air gap length which is set to 1.0 mm in all AFPMs in this article and B_r is the remanence of permanent magnet. The remanence of the Nd-bonded PM used in AFPMs is approx. 0.8 T. The DSSR-AFPM and the proposed T-AFPM have air gaps on both sides of the magnet, and this corresponds to $g = 2.0$ mm in (2). Fig. 8 shows the air gap magnetic flux density B_g for each magnet thickness t_{pm} calculated using (2) for $g = 1.0$ and 2.0 mm. On the graph for $g = 2.0$ mm, the DSSR-AFPM and the proposed T-AFPM have t_{pm} of 1.5 and 3.7 mm, respectively. As a result, the proposed T-AFPM can achieve a 53% higher air gap magnetic flux density. In contrast, the SSSR-AFPM has only one air gap, and its B_g can be predicted on the graph for $g = 1.0$ mm ($t_{pm} = 1.5$ mm). As a result, its air gap magnetic flux density can be made to be similar to that of the proposed T-AFPM.

Fig. 9 shows the air gap magnetic flux density of the proposed T-AFPM under no-load condition. The fundamental amplitude is 0.56 T which is in good agreement with the predicted value by (2). In this article, the torque factor T_{fct} is defined as follows:

$$T_{fct} = B_g S_{pm} F \tag{3}$$

where F is the magnetomotive force of the winding, which is the product of the armature current and the number of turns. In general, as T_{fct} increases, the average torque also increases. Fig. 10 compares the average torque obtained by 3-D-FEA and torque factor T_{fct}, in the four AFPMs. The trends of the average torque and torque factor are almost the same. The SSSR-AFPM has larger S_{pm} than that of the proposed T-AFPM, but its B_g and F are smaller. As a result, there is no large difference of T_{fct} between SSSR-AFPM and the proposed T-AFPM, leading to almost the same average torque. The difference of T_{fct} between the two DSSR-AFPMs is caused by only the difference of F.

The torque factor T_{fct} cannot perfectly predict the torque, and the actual torque is affected by various factors such as the structure and magnetic saturation. For example, the average torque of the proposed T-AFPM decreases because there is some leakage magnetic flux next to the C-type core. Furthermore, the power factor of the proposed T-AFPM is reduced due to this leakage flux. The power factors of the SSSR-AFPM, DSSR-AFPM-1, DSSR-AFPM-2, and the proposed T-AFPM are 0.9, 0.93, 0.85, and 0.71, respectively. The power factor of the proposed T-AFPM is the lowest. However, this power factor of the proposed T-AFPM can achieve the target output power of 700 W without any problems because general-purpose inverters of several kVA are typically employed in industrial applications such as water pumps. Eventually, in an ultra-flat shape, the proposed T-AFPM with a C-type core can achieve the target output power of 700 W and the lowest torque ripple simultaneously.

C. Mechanical Strength and Axial Force

Fig. 11 shows the results of structural analyses of the DSSR-AFPM and the proposed T-AFPM at the maximum rotational

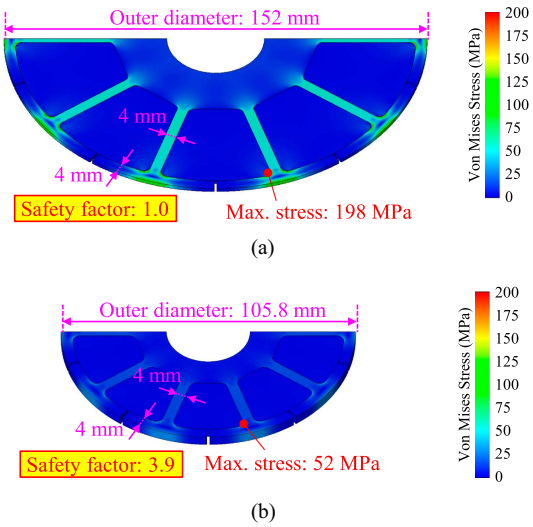

Fig. 11. Von mises stress distributions at maximum rotational speed of 6000 rpm. (a) DSSR-AFPM. (b) Proposed T-AFPM.

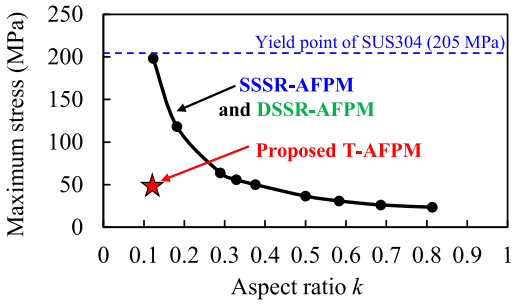

Fig. 12. Maximum von mises stress generated in the rotor for each model with different aspect ratio (at 6000 rpm).

speed of 6000 rpm. The maximum stress of the DSSR-AFPM almost reaches the yield point (205 MPa) of the PM holder made of SUS304, whereas the proposed T-AFPM has a sufficient safety factor for the rotor. This is because the proposed T-AFPM has a stator on the outside, resulting in a smaller rotor diameter. Additionally, the rotor diameter of the SSSR-AFPM is the same as that of the DSSR-AFPM, which is disadvantageous in terms of mechanical strength.

Fig. 12 shows the maximum stress generated in the rotor at 6000 rpm for each aspect ratio of the DSSR-AFPM. For all models, the maximum stress occurs in the PM holder. The flatter the rotor, the larger the rotor diameter, and therefore the higher the maximum stress. Therefore, if the SSSR- and DSSR-AFPMs are made even flatter than $k = 0.12$, the safety factor against centrifugal force becomes less than 1.0. In contrast, the proposed T-AFPM has sufficient mechanical strength even at an aspect ratio of $k = 0.12$, meaning that it is possible to make it even flatter.

A concern with AFPMs is the risk of contact between the disk-shaped rotor and stator due to eccentricity, as shown schematically in Fig. 13 [20], [21]. The outer diameter of the SSSR-AFPM and the DSSR-AFPM rotor is 152 mm, which

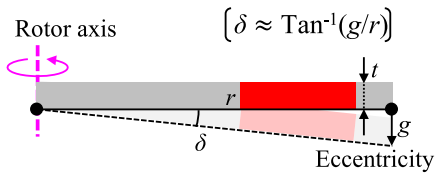

Fig. 13. Schematic representation of static and dynamic eccentricity of the rotor in AFPMs.

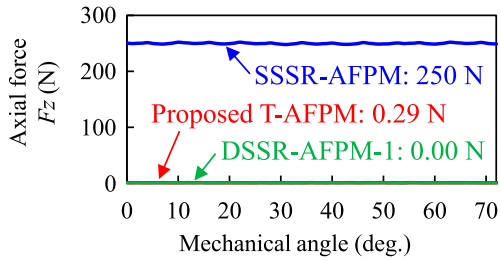

Fig. 14. Comparison of axial force F_z in the rotor between SSSR-AFPM, DSSR-AFPM, and the proposed T-AFPM (@6000 rpm, 4.0 Arms/mm^2).

is larger than that of the T-AFPM (105.8 mm). Therefore, the acceptance limit of the deviation angle δ in the SSSR- and DSSR-AFPM is 0.75°, whereas in the proposed T-AFPM it is 1.08° i.e., 44% higher. This means that the proposed T-AFPM has better manufacturability and better stability during operation.

Fig. 14 shows the axial force of the SSSR-AFPM, DSSR-AFPM, and the proposed T-AFPM at the rated current density. The SSSR-AFPM has very large axial force of 250 N, causing a large mechanical loss and noise. This axial force is caused by the asymmetric structure of the SSSR-AFPM in the axial direction. Additionally, a large S_{pm} of the SSSR-AFPM due to the ultra-flat shape causes an increase in the axial force. In contrast, the DSSR-AFPM and proposed T-AFPM can effectively suppress the axial force in the rotor because of their symmetric structure in the axial direction.

D. Loss and Efficiency

In this section, the loss and efficiency of the conventional AFPMs and the proposed T-AFPM are compared using 3-D-FEA. Rectangular windings give a higher coil space factor but are likely to increase eddy current loss because of their larger surface area. For DSSR-AFPM-2, much leakage magnetic flux passes through the rectangular windings because they are near both sides of the PMs; this means that large eddy currents can occur, especially at high speed. Eddy currents in the windings can be restrained by using tooth-tips on the stator teeth [31], but that approach is very difficult with an ultra-flat shape because of its thinness. Also, using tooth-tips is disadvantageous regarding manufacturability and cost.

Fig. 15 shows the magnetic paths on two cross sections from A′ to B′, and from C′ to D′ in the proposed T-AFPM. From this figure, it is clear that in the proposed T-AFPM, basically no magnetic flux passes through the rectangular windings. In this way, the proposed T-AFPM with a C-type core limits any eddy current despite having rectangular windings.

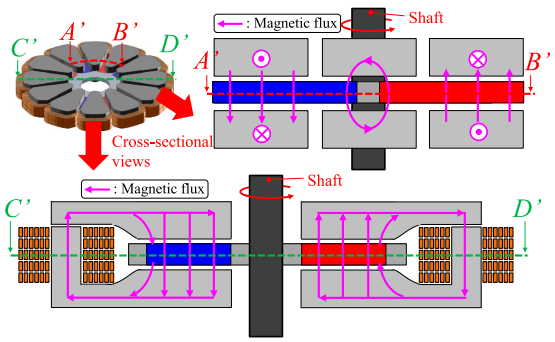

Fig. 15. Magnetic flux paths that might generate the eddy current loss in the winding. (a) DSSR-AFPM-2. (b) Proposed T-AFPM.

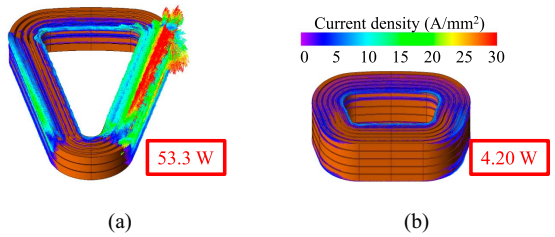

Fig. 16. Eddy current density distributions at rated current density and maximum rotational speed (4.0 Arms/mm^2, 6000 rpm).

Fig. 16 shows the eddy current density distributions in the rectangular windings of DSSR-AFPM-2 and the proposed T-AFPM at 6000 rpm and 4.0 Arms/mm^2. An extremely large eddy current loss occurs in the windings of DSSR-AFPM-1 because it has rectangular windings and much leakage magnetic flux passes through them, as mentioned earlier. By contrast, although the proposed T-AFPM has rectangular windings, its eddy current loss is markedly small at 4.2 W because little magnetic flux passes through the windings on its C-type core as shown in Fig. 15. From the above, the proposed T-AFPM with a C-type core overcomes the drawbacks of having rectangular windings. Fig. 17 shows the distributions of magnetic flux density in the stator core of the DSSR-AFPM-2 and the proposed model. Both models have a maximum magnetic flux density of more than 1.5 T in the stator back yoke because of their ultra-flat shape.

Fig. 18 shows the efficiency and breakdown of losses in the four comparative models at 4.0 Arms/mm^2 and 6000 rpm. The net losses and efficiency in the four models are compared in Fig. 18(a). Although all models have the same current density of 4.0 Arms/mm^2, they differ in their copper loss for the following two reasons: the round and rectangular copper wires have different cross-sectional areas (i.e., the magnitude of the applied current differs with the winding type), and the winding resistance differs among the four models.

DSSR-AFPM-2 has the largest eddy current loss in the windings, whereas that of DSSR-AFPM-1 is markedly small because of its round copper wires. Consequently, the efficiency of the DSSR-AFPM-2 is the lowest of 87.5% in the three models, and the heat generation in its windings is predicted to be very

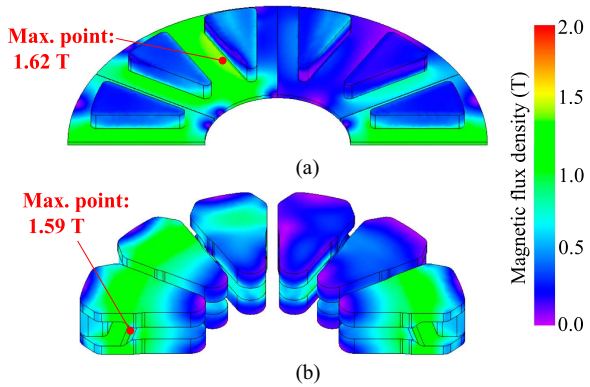

Fig. 17. Magnetic flux density distributions in the stator core at rated current density and maximum rotational speed (4.0 Arms/mm^2, 6000 rpm). (a) DSSR-AFPM-2. (b) Proposed T-AFPM.

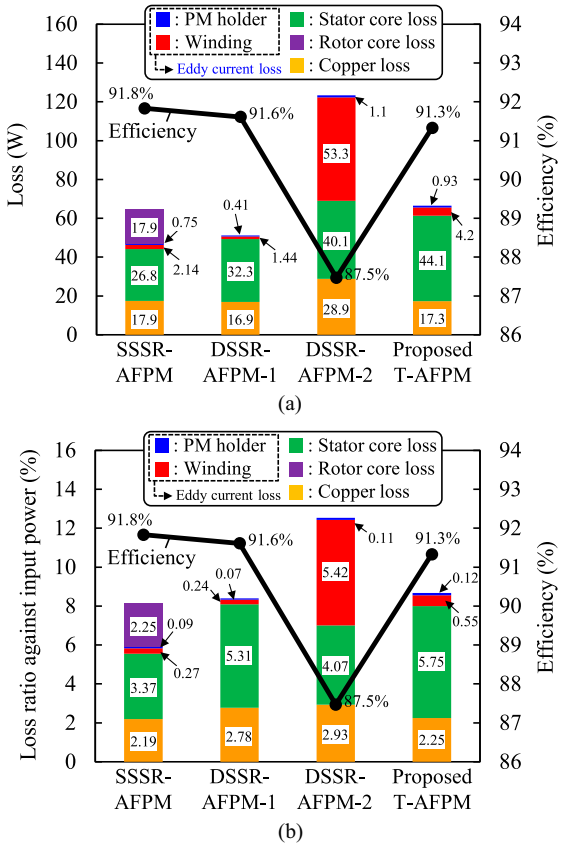

Fig. 18. Efficiency and breakdown of losses (@4.0 Arms/mm^2, 6000 rpm). (a) Net losses. (b) Loss ratio against input power.

large. By contrast, DSSR-AFPM-1 has the lowest total loss, but it cannot achieve the target power of 700 W at 6000 rpm. The proposed T-AFPM has a total loss that is 30.1% larger than that of DSSR-AFPM-1, but DSSR-AFPM-1 has a lower average torque, and so as shown in Fig. 18(b), both models have almost the same ratio of total loss to input power. The SSSR-AFPM achieves the highest efficiency of them because it has a large torque and only one stator core. However, the SSSR-AFPM has the largest rotor loss due to the rotor core. In AFPMs,

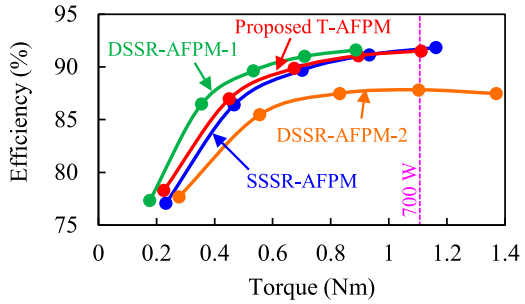

Fig. 19. Comparison of efficiency in the four AFPMs at maximum rotational speed of 6000 rpm.

even though loss is small, the volume of the disk-shaped rotor is small, resulting in large heat generation [49]. In the SSSR-AFPM, about one-quarter of the input power becomes losses in the rotor, making it unsuitable for continuous operation in the high-speed range.

Fig. 19 shows the efficiency of the four AFPMs at the maximum speed of 6000 rpm when the armature current is changed. DSSR-AFPM-2 has the lowest efficiency due to the eddy current loss in the winding, especially in large-torque areas. DSSR-AFPM achieves high efficiency in low-torque areas, but its torque does not meet the required output power. The proposed T-AFPM and SSSR-AFPM have the almost same efficiency and maximum torque which meets the requirements.

Fig. 20 shows the efficiency and rotor loss of the four AFPMs as the rotational speed increases when the rated current density of 4.0 Arms/mm^2 is applied. In all areas, DSSR-AFPM-2 indicates the lowest efficiency. Its efficiency dramatically decreases at high speed due to the eddy current loss in winding. The SSSR-AFPM achieves high efficiency in low-speed areas, but its efficiency decreases as rotational speed increases because the rotor loss is extremely large, as shown in Fig. 20(b). The magnetic flux density distribution of the SSSR-AFPM is also included in Fig. 20(b), the rotor back core shows high magnetic flux density causing large iron loss. The proposed T-AFPM achieves both high efficiency and low rotor loss at maximum speed of 6000 rpm, meaning that its property is suitable for continuous operation while maintaining the required power of 700 W.

E. Durability Against Demagnetization

Nd-bonded PMs have non-linear hysteresis characteristics, and so irreversible demagnetization easily occurs. Therefore, it is very important to minimize the demagnetization ratio of such magnets. Fig. 21 shows the distributions of irreversible demagnetization ratio in each of the comparative models. In each case, it is clear that the PMs in the part facing the teeth are greatly demagnetized. In the two DSSR-AFPMs, the surface area of the teeth is narrower than that in the proposed T-AFPM and so it is easier for a diamagnetic field to build up against the PMs. Moreover, as mentioned earlier, the PMs in the two DSSR-AFPMs are very thin because of the DSSR structure. Consequently, the maximum demagnetization ratio for DSSR-AFPM-1 and DSSR-AFPM-2 is 2.48% and 5.15%,

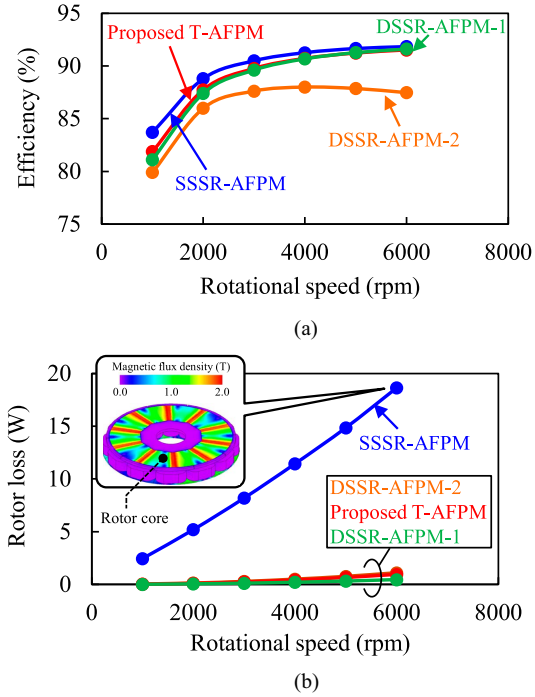

Fig. 20. Comparison of properties of the four AFPMs against rotational speed when applying rated current density of 4.0 Arms/mm^2. (a) Efficiency. (b) Rotor loss.

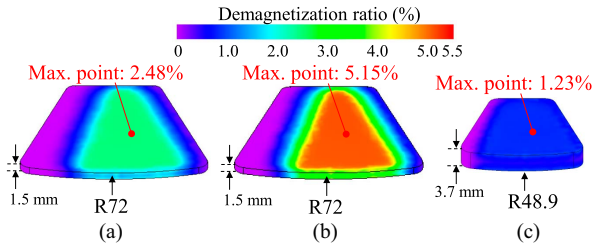

Fig. 21. Demagnetization ratio distributions in Nd-bonded PM after applying rated current density of 4.0 Arms/mm^2. (a) DSSR-AFPM-1. (b) DSSR-AFPM-2. (c) Proposed T-AFPM.

respectively, each of which is higher than that for the proposed T-AFPM. Therefore, the proposed T-AFPM achieves the lowest demagnetization ratio of them because of its relatively thick PMs and wide surface area of teeth. Fig. 22 shows the reduction in flux linkage after applying d-axis current in the three models. The proposed T-AFPM is the most resistant to demagnetization, even at currents exceeding the rated value.

F. Summary of Comparisons

As a result of the comprehensive comparison of the four AFPMs, the SSSR-AFPM and the proposed T-AFPM show excellent overall performance in the ultra-flat structure with an aspect ratio of $k = 0.12$. However, the SSSR-AFPM has many issues in terms of structure, mechanical strength, and manufacturing, making it impractical for the ultra-flat structure of this article. The same issues remain for the DSSR-AFPM. For example, the SSSR-AFPM experiences a large axial force,

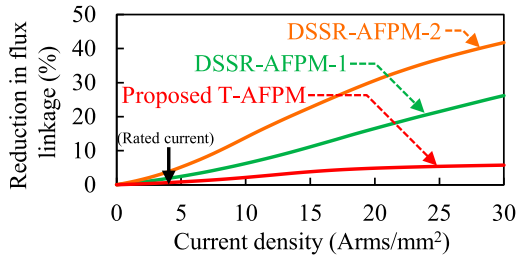

Fig. 22. Reduction in flux linkage after applying d-axis current i_d.

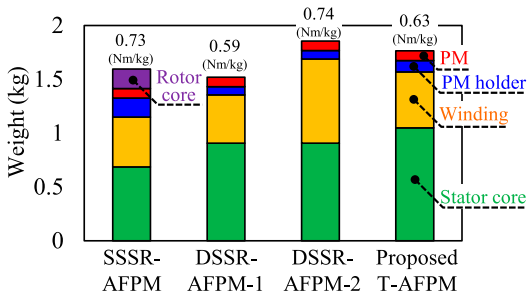

Fig. 23. Weight comparison of the four AFPMs.

causing noise and a short bearing lifetime, and it has a thin rotor back core, leading to low manufacturability. The two DSSR-AFPMs have a very thin stator back yoke made of SMC, meaning that they are difficult to build. DSSR-AFPM-1 with round wires cannot achieve the required output power of 700 W because of its low magnetomotive force, and DSSR-AFPM-2 with rectangular wires can generate an output power of at least 700 W but has the lowest efficiency because of the eddy current loss in its windings. Furthermore, the AFPM models have a rotor diameter that is larger than that of the proposed T-AFPM, and so the acceptance limit of their deviation angle is smaller, leading to lower stability during operation and poorer manufacturability. Additionally, the mechanical safety factor of their rotors is much lower than that of the proposed T-AFPM, and the demagnetization ratio of their Nd-bonded PMs is also lower than that of the proposed T-AFPM.

Meanwhile, the proposed T-AFPM overcomes the above problems with an ultra-flat shape, as mentioned earlier. It achieves high efficiency and a highly manufacturable structure while maintaining the required output power despite its ultra-flat shape with an axial length of 19.7 mm. The weight of the proposed T-AFPM is slightly larger than the SSSR-AFPM and DSSR-AFPM-1, as shown in Fig. 23. On the other hand, conventional AFPMs have issues with manufacturability, mechanical strength, and efficiency. Hence, the proposed T-AFPM can be said to be the lowest cost practical model with an ultra-flat structure.

IV. Experimental Results for Proposed T-AFPM

Fig. 24 shows a prototype of the proposed T-AFPM. The C-type core has two components as shown in Fig. 24(a) and (b). Fig. 24(c) shows the rotor with Nd-bonded PMs and the coreless

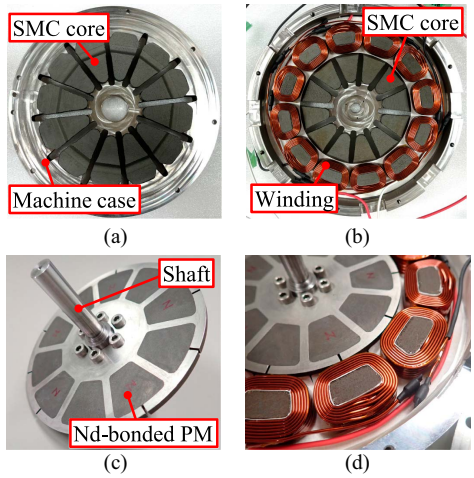

Fig. 24. Prototype of proposed T-AFPM. (a) Stator 1. (b) Stator 2. (c) Coreless rotor. (d) Assembled rotor and stator 2.

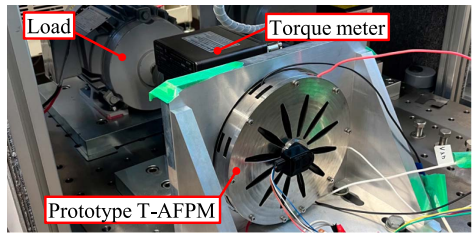

Fig. 25. Test platform and prototype of proposed T-AFPM.

rotor structure, leading to a flat shape and low eddy current loss. The rotor is inserted in the stator as shown in Fig. 24(d). Fig. 25 shows the test platform used for experimenting on the prototype T-AFPM. The torque and efficiency are measured using a torque meter (TH-2504, Ono Sokki Company Ltd.), and a power meter (WT1800, Yokogawa Test & Measurement Company Ltd.), respectively.

Fig. 26 shows the induced voltage waveform of the proposed T-AFPM under no-load condition at low-speed, and compares the 3-D-FEA and measured value. Both sets of results agree well, meaning that the prototype was manufactured highly accurately. Fig. 27 compares the FEA-predicted and the measured torque characteristics at the low speed of 1000 rpm. As a result of the high accuracy of the no-load voltage, the measured torque also has a small error compared to the 3-D-FEA, and the proposed T-AFPM satisfies the required torque performance even in the prototype.

Fig. 28 compares the cogging and rated torque waveforms measured on the prototype with the 3-D-FEA results. To improve measurement accuracy, the waveforms are measured at a very low speed of 50 rpm. The rated torque waveform has clearly larger ripples. The main causes are thought to be variations in the height of the SMC core manufactured by cutting processing and variations in the adhesive between the SMC core and the machine case. These issues are likely to be resolved in the case of mass production using die pressing.

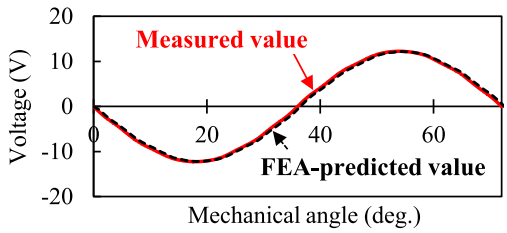

Fig. 26. Comparison of no-load back-EFM waveforms between 3-D-FEA and experimental results (@1000 rpm).

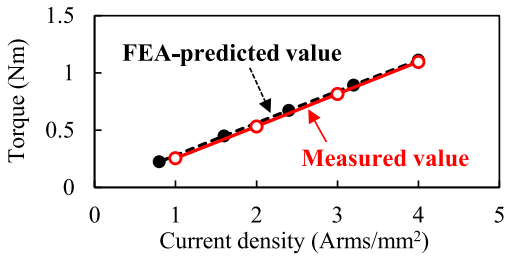

Fig. 27. Comparison of torque versus current density characteristics between 3-D-FEA and experimental results (@1000 rpm).

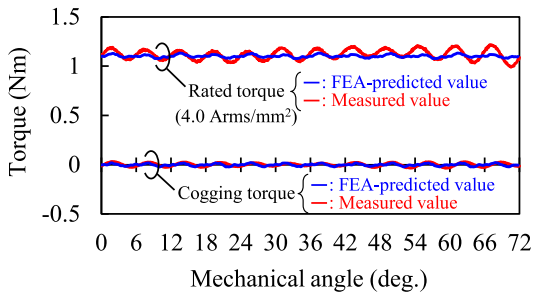

Fig. 28. Cogging and rated torque waveforms at 50 rpm.

Figs. 29 and 30 compare the FEA-predicted and measured maps of iron loss and efficiency of the proposed T-AFPM. The measured iron loss increases over the entire operating range. This is because the three-phase inverter is driven using PWM control with a switching frequency of 10 kHz in the experiment. The efficiencies on both maps increase with increasing torque and rotational speed. The efficiency trends of both maps are the same, but the measured values are generally lower due to the increase in iron loss. The maximum efficiency, which is 91.3% in the FEA-predicted map, dropped to 89.5% in the prototype. However, the prototype T-AFPM achieved IE5-class efficiency at high speed and torque, which is the region targeted in this research.

Fig. 31 shows the measured thermal characteristics of the proposed T-AFPM. Fig. 31(a) shows the locations of the five thermocouples installed in the stator. Fig. 31(b) indicates the temperature distribution after continuous operation of the prototype at the rated operating point (6000 rpm, 4.0 Arms/mm^2). Fig. 31(b) also shows the location of the sixth thermocouple for

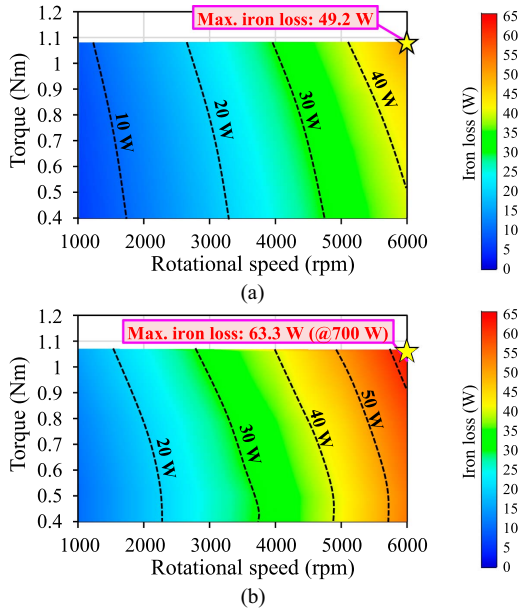

Fig. 29. Iron loss maps of proposed T-AFPM. (a) 3-D-FEA result. (b) Measured results.

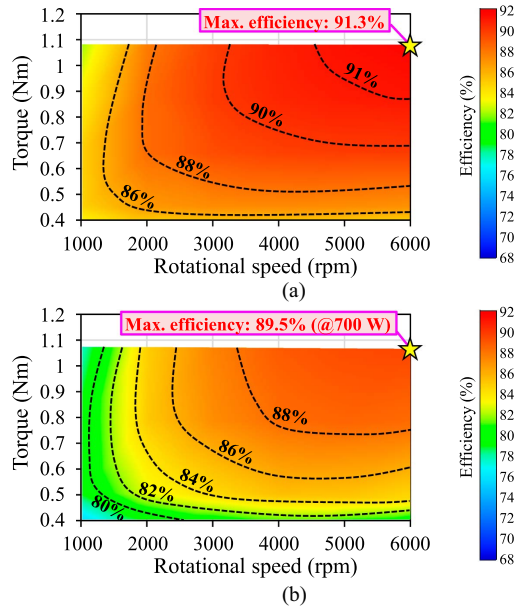

Fig. 30. Efficiency maps of proposed T-AFPM. (a) 3-D-FEA result. (b) Measured results.

measuring the case temperature. Fig. 31(c) shows the temperature measured by the six thermocouples. After operating for more than 1 h, each part is almost the thermal steady state, and the maximum temperature is approximately 48.7 °C between the coils. Therefore, the proposed T-AFPM can continuously operate in the high-speed area without cooling, despite its ultra-flat shape. As shown in Fig. 31(b), the rotor temperature is measured from a hole in the case and is below 40 °C. The Nd-bonded PM suppresses rotor loss and contributes to reducing the temperature.

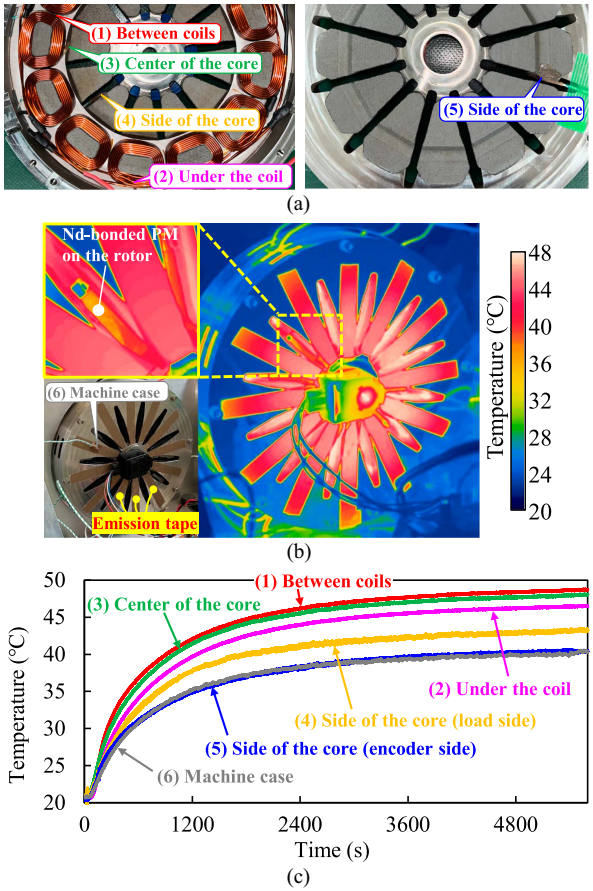

Fig. 31. Thermal characteristics of the proposed T-AFPM at rated point (6000 rpm, 4.0 Arms/mm^2). (a) Installation points of thermocouples. (b) Temperature distribution under continuous operation. (c) Temperature measured by thermocouples.

V. Conclusion

This article proposed an ultra-flat T-AFPM with a C-type SMC core for industrial applications. First, this article considered the performance of the proposed T-AFPM and conventional AFPMs in an ultra-flat structure based on some parameters such as the magnet structural parameters and air gap length. For comparisons with conventional AFPMs, the proposed AFPM has many better characteristics such as its efficiency, manufacturability, mechanical strength, and stability.

Experimental verification of the proposed T-AFPM was also carried out, and the prototype T-AFPM showed the highest efficiency of 89.5% at 6000 rpm and 700 W point. Consequently, the proposed T-AFPM can realize high efficiency at high speed and the target output power of 700 W despite its ultra-flat shape with an axial length of 19.7 mm. Additionally, the prototype showed small cogging torque and achieved continuous operation at rated operating point without cooling. Therefore, the proposed T-AFPM is a very good candidate for reduced system size in industrial applications.

References

[1] A. De Almeida et al., "EuP lot 11 motors, ecodesign assessment of energy using products," ISR-Univ. Coimbra, Brussels, Belgium, Final Report for the European Commissions, Feb. 2008.

[2] H. Qin et al., "Differential evolutionary modeling and starting-up cavitation characteristics analysis for multistage centrifugal pump," in *Proc. IEEE 4th Inf. Technol. Mechatron. Eng. Conf. (ITOEC)*, 2018, pp. 412–416.

[3] A. De Almeida, F. Ferrieira, and G. Baoming, "Beyond induction motors—Technology trends to move up efficiency," *IEEE Trans. Ind. Appl.*, vol. 50, no. 3, pp. 2103–2114, May/Jun. 2014.

[4] T. Husain et al., "A comprehensive review of permanent magnet transverse flux machines: Use in direct-drive applications," *IEEE Ind. Appl. Mag.*, vol. 26, no. 6, pp. 87–98, Nov./Dec. 2020.

[5] R. Tsunata, M. Takemoto, S. Ogasawara, T. Ueno, and T. Saitoh, "A proposal of ultra-flat axial gap motor employing C-type SMC core," in *Proc. 45th Annu. Conf. IEEE Ind. Electron. Soc. (IECON)*, 2019, pp. 874–879.

[6] Y. Kano, T. Kosaka, and N. Matsui, "A simple nonlinear magnetic analysis for axial-flux permanent-magnet machines," *IEEE Trans. Ind. Electron.*, vol. 57, no. 6, pp. 2124–2133, Jun. 2010.

[7] J.-Y. Lee et al., "Design of an axial flux permanent magnet generator for a portable hand crank generating system," *IEEE Trans. Magn.*, vol. 48, no. 11, pp. 2977–2980, Nov. 2012.

[8] J. Lai, J. Li, and T. Xiao, "Design of a compact axial flux permanent magnet machine for hybrid electric vehicle," *IEEE Trans. Ind. Electron.*, vol. 68, no. 8, pp. 6630–6639, Aug. 2021.

[9] R. Benlamine et al., "3-D numerical hybrid method for PM Eddy-current losses calculation: Application to axial-flux PMSMs," *IEEE Trans. Magn.*, vol. 51, no. 7, pp. 1–10, Jul. 2015.

[10] M. F. H. Khatab, Z. Q. Zhu, H. Y. Li, and Y. Liu, "Comparative study of novel axial flux magnetically geared and conventional axial flux permanent magnet machines," *CES Trans. Elect. Machines Syst.*, vol. 2, no. 4, pp. 392–398, Dec. 2018.

[11] B.-O. Tak and J.-S. Ro, "Analysis and design of an axial flux permanent magnet motor for in-wheel system using a novel analytical method combined with a numerical method," *IEEE Access*, vol. 8, pp. 203994–204011, 2020.

[12] N. Taran, V. Rallabandi, G. Heins, and D. M. Ionel, "Coreless and conventional axial flux permanent magnet motors for solar cars," *IEEE Trans. Ind. Appl.*, vol. 54, no. 6, pp. 5907–5917, Nov./Dec. 2018.

[13] S. Khan et al., "Design and analysis of a 4-kW two-stack coreless axial flux permanent magnet synchronous machine for low-speed applications," *IEEE Access*, vol. 7, pp. 173848–173854, 2019.

[14] R. Burke, A. Giedymin, Z. Wu, H. Chuan, N. Bourne, and J. G. Hawley, "A lumped parameter thermal model for single-sided AFPM machines with experimental validation," *IEEE Trans. Transp. Electrific.*, vol. 6, no. 3, pp. 1065–1083, Sep. 2020.

[15] M. Shokri, N. Rostami, V. Behjat, J. Pyrhönen, and M. Rostami, "Comparison of performance characteristics of axial-flux permanent-magnet synchronous machine with different magnet shapes," *IEEE Trans. Magn.*, vol. 51, no. 12, pp. 1–6, Dec. 2015.

[16] NuGen Mobility Inc., *SCM150-XXX Axial Flux, Brushless PM Motor Specifications*. Ashburn, VA, USA: New Generation Motors Corporation, 2007.

[17] H. Vansompel, A. Rasekh, A. Hemeida, J. Vierendeels, and P. Sergeant, "Coupled electromagnetic and thermal analysis of an axial flux PM machine," *IEEE Trans. Magn.*, vol. 51, no. 11, pp. 1–4, Nov. 2015.

[18] T.-S. Kwon, S.-K. Sul, L. Alberti, and N. Bianchi, "Design and control of an axial-flux machine for a wide flux-weakening operation region," *IEEE Trans. Ind. Appl.*, vol. 45, no. 4, pp. 1258–1266, Jul./Aug. 2009.

[19] F. Marignetti, V. Delli Colli, and Y. Coia, "Design of axial flux PM synchronous machines through 3-D coupled electromagnetic thermal and fluid-dynamical finite-element analysis," *IEEE Trans. Ind. Electron.*, vol. 55, no. 10, pp. 3591–3601, Oct. 2008.

[20] O. O. Ogidi, P. S. Barendse, and M. A. Khan, "Detection of static eccentricities in axial-flux permanent-magnet machines with concentrated windings using vibration analysis," *IEEE Trans. Ind. Appl.*, vol. 51, no. 6, pp. 4425–4434, Nov./Dec. 2015.

[21] S. M. Mirimani et al., "Effect of inclined static eccentricity fault in single stator-single rotor axial flux permanent magnet machines," *IEEE Trans. Magn.*, vol. 48, no. 1, pp. 143–149, Jan. 2012.

[22] N. S. S. P. Nikam et al., "Performance comparison between PCB-stator and laminated-core-stator-based designs of axial flux permanent magnet motors for high-speed low-power applications," *IEEE Trans. Ind. Electron.*, vol. 67, no. 7, pp. 5269–5277, Jul. 2020.

[23] E. Ajily et al., "Three-dimensional field reconstruction method for modeling axial flux permanent magnet machines," *IEEE Trans. Energy Convers.*, vol. 30, no. 1, pp. 199–207, Mar. 2015.

[24] W. Li et al., "Structural analysis of single-sided axial-flux permanent magnet machines with different magnetic materials," *IEEE Trans. Magn.*, vol. 57, no. 2, pp. 1–5, Feb. 2021.

[25] F. Zhao, T. A. Lipo, and B.-I. Kwon, "A novel dual-stator axial-flux spoke-type permanent magnet vernier machine for direct-drive applications," *IEEE Trans. Magn.*, vol. 50, no. 11, pp. 1–4, Nov. 2014.
[26] S. Javadi and M. Mirsalim, "Design and analysis of 42-V coreless axial-flux permanent-magnet generators for automotive applications," *IEEE Trans. Magn.*, vol. 46, no. 4, pp. 1015–1023, Apr. 2010.
[27] R. Tsunata, M. Takemoto, S. Ogasawara, A. Watanabe, T. Ueno, and K. Yamada, "Development and evaluation of an axial gap motor using neodymium bonded magnet," *IEEE Trans. Ind. Appl.*, vol. 54, no. 1, pp. 254–262, Jan./Feb. 2018.
[28] N. Li et al., "Hybrid-excited series permanent magnet axial field flux switching memory machine," *IEEE Trans. Appl. Supercond.*, vol. 29, no. 2, pp. 1–5, Mar. 2019.
[29] S. Khaliq et al., "Rotor pole optimization of novel axial-flux brushless doubly fed reluctance machine for torque enhancement," *IEEE Trans. Magn.*, vol. 52, no. 7, pp. 1–4, Jul. 2016.
[30] Y. Lu et al., "Six-phase double-stator inner-rotor axial flux PM machines with novel detached winding," *IEEE Trans. Ind. Appl.*, vol. 53, no. 3, pp. 1931–1941, May/Jun. 2017.
[31] R. Tsunata, M. Takemoto, J. Imai, T. Saito, and T. Ueno, "Superior efficiency under PWM harmonic current in an axial-flux PM machine for HEV/EV traction: Comparison with a radial-flux PM machine," *IEEE Trans. Ind. Appl.*, vol. 60, no. 5, pp. 6736–6751, Sep./Oct. 2024.
[32] Z. Zhang et al., "Feasibility of a new ironless-stator axial flux permanent magnet machine for aircraft electric propulsion application," *CES Trans. Elect. Machines Syst.*, vol. 3, no. 1, pp. 30–38, Mar. 2019.
[33] Y. C. Wang, W. N. Fu, and X. J. Li, "A novel axial flux stator and rotor dual permanent magnet machine," *CES Trans. Elect. Machines Syst.*, vol. 1, no. 2, pp. 140–145, 2017.
[34] S. Niu et al., "A novel axial-flux-complementary doubly salient machine with boosted PM utilization for cost-effective direct-drive applications," *IEEE Access*, vol. 7, pp. 145970–145977, 2019.
[35] L. Li, W. N. Fu, S. L. Ho, S. Niu, and Y. Li, "A quantitative comparison study of power-electronic-driven flux-modulated machines using magnetic field and thermal field co-simulation," *IEEE Trans. Ind. Electron.*, vol. 62, no. 10, pp. 6076–6084, Oct. 2015.
[36] J. Chang, Y. Fan, J. Wu, and B. Zhu, "A yokeless and segmented armature axial flux machine with novel cooling system for in-wheel traction applications," *IEEE Trans. Ind. Electron.*, vol. 68, no. 5, pp. 4131–4140, May 2021.
[37] M. Aydin, S. Huang, and T. A. Lipo, "Design, analysis, and control of a hybrid field-controlled axial-flux permanent-magnet motor," *IEEE Trans. Ind. Electron.*, vol. 57, no. 1, pp. 78–87, Jan. 2010.
[38] Y. Liu et al., "Design and analysis of oil-immersed cooling stator with nonoverlapping concentrated winding for high-power ironless stator axial-flux permanent magnet machines," *IEEE Trans. Ind. Electron.*, vol. 68, no. 4, pp. 2876–2886, Apr. 2021.
[39] S. M. Hosseini, M. Agha-Mirsalim, and M. Mirzaei, "Design, prototyping, and analysis of a low cost axial-flux coreless permanent-magnet generator," *IEEE Trans. Magn.*, vol. 44, no. 1, pp. 75–80, Jan. 2008.
[40] Y. Wang et al., "Development of a high-performance axial flux PM machine with SMC cores for electric vehicle application," *IEEE Trans. Magn.*, vol. 55, no. 7, pp. 1–4, Jul. 2019.
[41] B. Zhang, T. Seidler, R. Dierken, and M. Doppelbauer, "Development of a yokeless and segmented armature axial flux machine," *IEEE Trans. Ind. Electron.*, vol. 63, no. 4, pp. 2062–2071, Apr. 2016.
[42] W. Geng, J. Hou, and Q. Li, "Electromagnetic analysis and efficiency improvement of axial-flux permanent magnet motor with yokeless stator by using grain-oriented silicon steel," *IEEE Trans. Magn.*, vol. 58, no. 2, pp. 1–5, Feb. 2022.
[43] X. Wang et al., "Electromagnetic performance analysis of an axial flux hybrid excitation motor for HEV drives," *IEEE Trans. Appl. Supercond.*, vol. 31, no. 8, pp. 1–5, Nov. 2021.
[44] G. De Donato et al., "Fractional-slot concentrated-winding axial-flux permanent-magnet machine with core-wound coils," *IEEE Trans. Ind. Appl.*, vol. 48, no. 2, pp. 630–641, Mar./Apr. 2012.
[45] Y. Huang et al., "Magnetic equivalent circuit modeling of yokeless axial flux permanent magnet machine with segmented armature," *IEEE Trans. Magn.*, vol. 50, no. 11, pp. 1–4, Nov. 2014.
[46] R. Tsunata, M. Takemoto, S. Ogasawara, A. Watanabe, T. Ueno, and K. Yamada, "Investigation of enhancing efficiency and acceleration in a flat shape axial gap motor having high torque characteristic," in *Proc. IEEE Int. Conf. Mechatron. (ICM)*, Feb. 2017, pp. 278–283.
[47] R. Tsunata, M. Takemoto, S. Ogasawara, T. Saito, and T. Ueno, "SMC development guidelines for axial flux PM machines employing coreless rotor structure for enhancing efficiency based on experimental results," *IEEE Trans. Ind. Appl.*, vol. 58, no. 3, pp. 3470–3485, May/Jun. 2022.
[48] D. Azuma et al., "Investigation of the influence of harmonics on iron loss of soft magnetic composites," in *Proc. IEEE Int. Conf. Elect. Machines (ICEM)*, Valencia, Spain, pp. 1124–1129, 2022.
[49] R. Tsunata, M. Takemoto, J. Imai, T. Saito, and T. Ueno, "Comparison of thermal characteristics in various aspect ratios for radial-flux and axial-flux permanent magnet machines," *IEEE Trans. Ind. Appl.*, vol. 59, no. 3, pp. 3353–3367, May/Jun. 2023.

Ren Tsunata (Member, IEEE) joined as a Research Fellow with Okayama University, Okayama, Japan, in 2021, where he became an Assistant Professor with the Graduate School of Natural Science and Technology, in 2022, and has been a Research Associate Professor, since 2023.

Dr. Tsunata is a member of the Institute of Electrical Engineers of Japan and The Japan Society of Applied Electromagnetics and Machines. He was a recipient of IEEJ Excellent Presentation Awards, in 2017, 2020, 2022, 2023, and 2024, respectively; the Young Investigators Award from EVTeC2025, and the Electrical Machines Committee Prize Paper Award from the IEEE Industry Applications Society, in 2025.

Masatsugu Takemoto (Member, IEEE) joined Tokyo Institute of Technology, Tokyo, Japan, as a Research Associate with the Department of Electrical Engineering. In 2004, he joined Musashi Institute of Technology, Tokyo, as a Research Associate with the Department of Mechanical Systems Engineering, where he became a Lecturer, in 2005. In 2008, he joined Hokkaido University, Hokkaido, Japan, as an Associate Professor with the Graduate School of Information Science and Technology. Since 2020, he has been with Okayama University, Okayama, Japan, where he is a Professor with the Graduate School of Natural Science and Technology. His research interests include permanent magnet synchronous motors, axial gap motors, rare-earth-free motors, bearingless motors, and magnetic bearings.

Jun Imai (Member, IEEE) received the B.S., M.S., and Ph.D. degrees in electrical engineering from the Department of Electrical Engineering, Kyushu University, in 1987, 1989, and 1992, respectively.

He became a Lecturer with Okayama University, Okayama, Japan, in 2000 and has been an Associate Professor, since 2008.

Tatsuya Saito received the B.S., M.S., and Ph.D. degrees in material science from Tohoku University, Sendai, Japan, in 2009, 2011, and 2014, respectively.

Since 2014, he has been with Sumitomo Electric Industries Ltd., Hyogo, Japan. His research interests include soft magnetic materials and powder metallurgy.

Tomoyuki Ueno received the B.S. and M.S. degrees in mechanical engineering from Kobe University, Hyogo, Japan, in 1999 and 2001, respectively, and the Dr. Eng. degree in industrial innovation science from Okayama University, Okayama, Japan, in 2015.

Since 2001, he has been with Sumitomo Electric Industries Ltd., Hyogo, Japan. His research interest includes soft magnetic materials.